iScience

CellPress
OPEN ACCESS

Article

A nanowell-based MoS_2 neuroelectrode for high-sensitivity neural recording

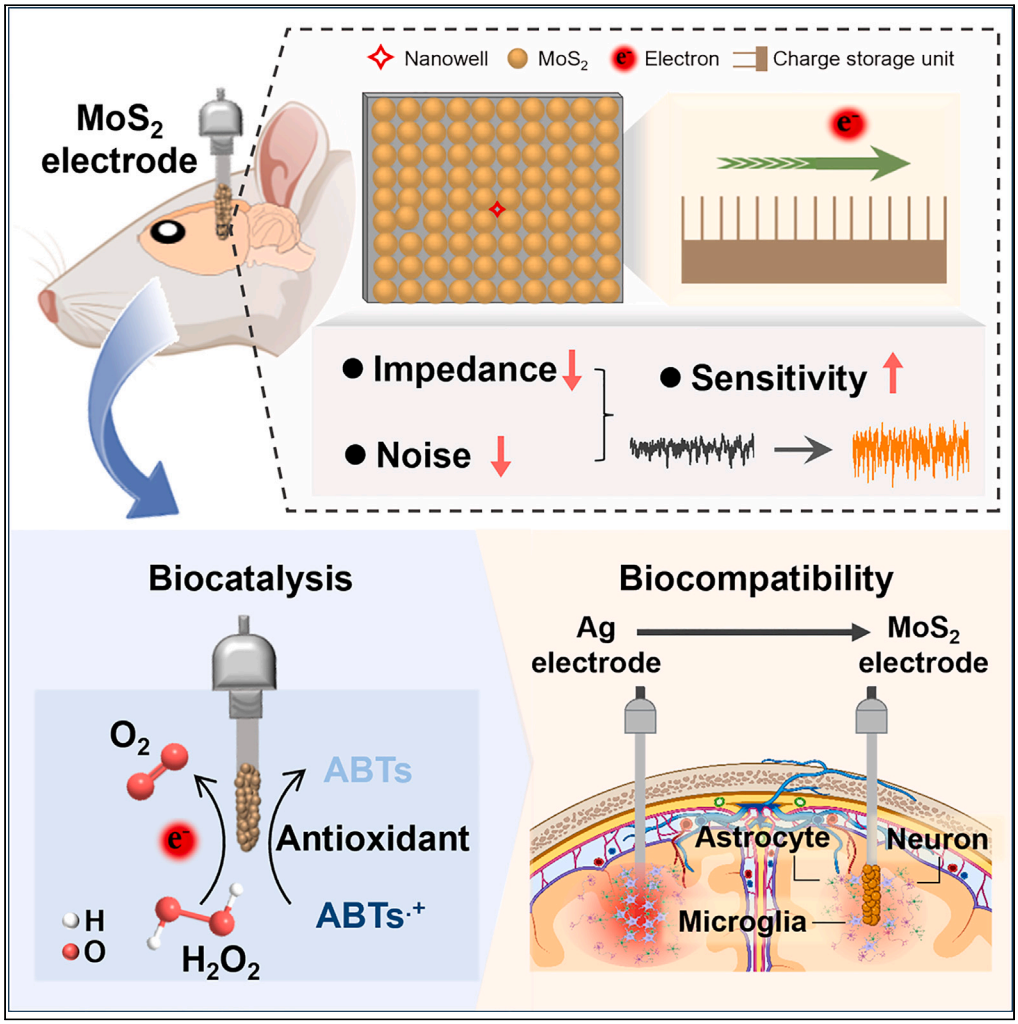

Shuangjie Liu, Xinyu Sun, Yang Wang, ..., Hao Wang, Xiao-Dong Zhang, Dong Ming

xiaodongzhang@tju.edu.cn (X.-D.Z.)
richardming@tju.edu.cn (D.M.)

Highlights

MoS_2 nanosheets form tiny nanowells on electrode act as quantized charge storage units

Recording sensitivity improved by lowering interfacial electron transport barriers

High bioactivity of MoS_2 electrodes greatly reduces the inflammatory response

Liu et al., iScience 27, 110949
October 18, 2024
https://doi.org/10.1016/j.isci.2024.110949

iScience

CellPress
OPEN ACCESS

Article

A nanowell-based MoS_2 neuroelectrode for high-sensitivity neural recording

Shuangjie Liu,[1,3] Xinyu Sun,[1,3] Yang Wang,[1] Kaijin Liu,[2] Renpeng Liu,[2] Yuqin Zhang,[1] Zhaoliang Ni,[1] Wanyu Tang,[1] Shaofang Zhang,[1] Xiaoyu Mu,[1] Hao Wang,[1] Xiao-Dong Zhang,[1,2,4,*] and Dong Ming[1,*]

SUMMARY

Implantable neural electrodes are crucial in neurological diagnosis and therapy because of their ultra-high spatial resolution, but they are constrained by high impedance and insufficient charge injection capacity, resulting in noise that often obscures valuable signals. Emerging nanotechnologies are powerful tools to improve sensitivity and biocompatibility. Herein, we developed quantized 2D MoS_2 electrodes by incorporating bioactive MoS_2 nanosheets onto bare electrodes, achieving sensitive, compatible recording. The 2D materials can create tiny nanowells, which behaved as quantized charge storage units and thus improved sensitivity. The key sensitivity indicators, impedance and cathode charge storage capacity, showed a multifold increase. The 17.7-fold improvement in catalytic activity of MoS_2 electrodes facilitated effective current transmission and reduced inflammatory response. *In vivo* recording showed that the sensitivity of local field potentials increased throughout frequency range and peaked at a 4.7-fold in β rhythm. This work provides a general strategy for achieving effective diagnoses of neurological disorders.

INTRODUCTION

Neural electrodes, as core devices for understanding the mechanism of information generation, transmission, and processing in the brain, have been widely used to record and stimulate neural activity.[1–6] As neural sensing devices with high spatial and temporal resolutions, implantable neural electrodes can realize signal exchange and transmission between the nervous system and external electronic systems, so they play a crucial role in the diagnosis and therapy of neurological disorders.[7–10] However, the useful signal of neural activities is weak and easily overwhelmed by background noise. The noise level in biosignal acquisition becomes unfavorable with increasing electrode impedance.[1,11,12] Moreover, current clinical electrodes are much more rigid than the host brain tissue, leading to the instability and deterioration of the tissue-electrode interface during prolonged implantation. Therefore, one of the design requirements of neural electrodes is to ensure low impedance at the electrode-brain tissue interface to guarantee a high signal-to-noise ratio (SNR),[13–16] and the size of the electrodes should be small enough to accurately extract and record electrical signals in the target neuron while reducing tissue damage.[17–20]

To maximize the contact area of the electrode with the electrolyte and thus improve the charge conduction density at a small size, researchers have exerted much effort to apply highly advanced nanotechnology for controlling and designing the surface morphology of electrodes.[21–26] Organic conducting polymers, particularly poly(3,4-ethylenedioxythiophene) (PEDOT), improve the electrical properties and bioactivity of neural electrodes, thereby enabling ameliorated electrode-tissue communication and long-term recording by reducing impedance and substantially enhanced charge injection capacity over time.[25] However, PEDOT undergoes chemical degradation caused by prolonged electrical stimulation, resulting in delamination and cracking and affecting the long-term stability of the electrodes.[27,28] Nanoparticles with a small size effect and excellent biocompatibility are also effective methods for modifying electrodes. For example, electroplated Au, platinum black, reactive sputtering TiN, and sputtered 3D iridium oxide can form controlled micro/nanostructures on the electrode surface to improve recording sensitivity by increasing the effective activation area and decreasing impedance. Carbon nanotubes and graphene fibers, which have high carrier mobility and good biocompatibility, have been modified into flexible neural electrodes, thus reducing electrode impedance while improving signal recording quality.[16,29–33] However, delamination or detachment during prolonged use that leads to electrode failure is a long-standing problem. Therefore, neural interfaces with low recording noise and sufficient stability need to be developed to improve signal quality.

In this work, we prepared a high-performance MoS_2 electrode by modifying the electrode surface with typical 2D transition metal MoS_2 nanosheets to form a functional film with a nanowell structure. MoS_2 is a novel 2D nanomaterial with excellent mechanical properties and high charge carrier mobility (no less than 200 $cm^2 V^{-1} S^{-1}$),[34] and it has been successfully implemented in sensors, transistors, nanocomposites, and

[1]Tianjin Key Laboratory of Brain Science and Neural Engineering, Academy of Medical Engineering and Translational Medicine, Tianjin University, Tianjin 300072, China
[2]Tianjin Key Laboratory of Low Dimensional Materials Physics and Preparing Technology, Institute of Advanced Materials Physics, School of Sciences, Tianjin University, Tianjin 300350, China
[3]These authors contributed equally
[4]Lead contact
*Correspondence: xiaodongzhang@tju.edu.cn (X.-D.Z.), richardming@tju.edu.cn (D.M.)
https://doi.org/10.1016/j.isci.2024.110949

biomedicine to enhance responsivity and sensitivity.[35–38] As a transition metal sulfide, MoS_2 has an S–Mo–S sandwich structure because of weak van der Waals interactions. Benefiting from the undercoordination of Mo–S at the edges, highly reactive edge sites that can maximize catalytic and charge transport efficiencies are exposed. The introduction of MoS_2 nanosheets into the electrode surface creates numerous tiny nanowells that can store charge, provide a high-speed path for charge transfer, and promote interfacial charge transfer, thus helping achieve low impedance and high cathodic storage charge capacity (CSCc). In addition, the catalytic activity and certain anti-inflammatory properties of MoS_2 nanosheets can improve biocompatibility. MoS_2 electrodes enhance the detection of local field potential (LFP) signals and histocompatibility and are expected to enable safe and effective neural recording and stimulation.

RESULTS

Design and structural properties of MoS_2 electrodes

MoS_2-based neural probes with Ag electrodes were fabricated and are shown in Figure 1A. Ultraviolet-visible (UV-vis) light showed the appearance of four distinct excitonic peaks (A, B, C, and D), indicating MoS_2 nanosheets with relatively large lateral dimensions[39] (Figure 1B). The electrodes were 200 μm in diameter and had sufficient mechanical strength for self-supporting implantation into the brain. Commercial Ag of the same size was used for comparison. The MoS_2 nanosheets were deposited on the Ag electrode surface via the multiple potential step method, and the effect of different deposition potentials on electrode performance was explored. As shown in Figure 1C, the step size was set to 2 s, and the response current increased linearly with the deposition potential. The performance of the neural electrodes was directly related to the intrinsic properties of the coating material and the surface topography of the electrodes. Scanning electron microscope (SEM) images showed that the commercial Ag electrodes had a flat and smooth surface, and the MoS_2 electrodes' surface was densely covered by a MoS_2 layer with a uniform size and structural order. The MoS_2 layer became increasingly dense and small with increasing deposition potentials (Figure 1D). The atomic force microscope (AFM) results of the MoS_2 electrodes showed that the thickness of the MoS_2 functional layer was 691.04 $\pm$ 1.1 nm (Figure S1), and the cross-sectional SEM results revealed that the layer was tightly bonded to the substrate at the interface without voids or delamination (Figure S2). Elemental mapping (Figure 1E) and the Mo content (Figure 1F) showed that MoS_2 was uniformly distributed on the Ag electrode surface and the Mo content increased linearly with the deposition potentials. High deposition potentials provided high electric field strength, resulting in a high-energy state on the electrode surface and strong electrolyte flow. At the same time, the generated energy threshold was reduced, prompting the ions to deposit rapidly on the surface of the electrode to form a small-size, uniform MoS_2 layer, thereby exposing the effective reaction area for neural signal conduction.

X-ray diffraction (XRD) was performed to determine the crystal structure of the MoS_2 electrodes. Compared with the Ag electrodes' distribution on the (111) crystal plane, the Ag electrodes' peak position distribution in the MoS_2 electrodes did not shift, and the typical characteristic diffraction peaks of MoS_2 were observed in the samples at 29° and 36° (Figure 1G). In addition, the MoS_2 electrodes exhibited a strong diffraction peak at $2\theta = 29°$, which corresponded to the (100) crystal plane of MoS_2, indicating that MoS_2 was successfully deposited on the Ag surface. The surface layer compositions and the corresponding chemical valence of the elements in the MoS_2 electrodes were further evaluated via X-ray photoelectron spectroscopy (XPS) analysis. As shown in Figure 1H, the samples were mainly composed of Ag, Mo, S, and O elements; these results are in line with the energy-dispersive X-ray spectroscopy mapping results and prove the existence of MoS_2 on the surface of the Ag electrodes. The high-resolution XPS profiles of Mo 3d and S 2p were finely fitted to multiple deconvolution peaks (Figures 1I and 1J) to analyze the bonding state of the Mo and S elements of the MoS_2 electrodes. Typical Mo^{4+} $3d_{3/2}$ peaks at 232.8 eV and Mo^{4+} $3d_{5/2}$ peaks at 229.6 eV could be clearly seen, suggesting the presence of Mo (IV).[40] The binding energy of sulfur with the S $2p_{3/2}$ and S $2p_{5/2}$ peaks at 162.9 and 164.2 eV was consistent with the −2 oxidation state of sulfur.

Electrical properties and catalytic activity of the MoS_2 electrodes

The introduction of the MoS_2 nanosheets onto the electrode surface created numerous tiny nanowells that could store charge. According to the SEM results (Figure 1D), as the deposition potential increased, the pore size of the nanowells decreased, whereas their density increased substantially, forming quantized charge storage units (Figure 2A). The different deposition potentials resulted in various surface morphologies of the electrodes and surface roughness, which directly reflected the actual surface where the active chemical reaction occurred between the electrode and electrolyte. The 3D AFM images in Figure 2B show different morphologies with progressive undulations of the electrode surface under different deposition potentials. These results are in good agreement with the SEM results. The surface roughness of the MoS_2 electrodes increased from the initial 5.3 nm–107.3 nm, and the corresponding effective reaction surface was improved by 20.2 times, which was beneficial for achieving high charge storage capacity and low impedance. The electrodes were physically roughened to obtain an activated electrode surface and improve the deposition sites of the MoS_2 nanosheets and the bonding force between the functional film layer and the substrate. The roughened electrodes exhibited an initial improvement in electrochemical performance of more than 10% because of the exposure of numerous active sites and the consequent increase in the effective reactive area (Figure S3). The Bode plots in Figures 2C and 2D show that the impedance of the MoS_2 electrodes was much lower than that of the bare electrodes in the frequency ranges tested (1–100 kHz), and the impedance value decreased as the nanowells became densely packed. Simultaneously, the phase angle increased and gradually approached 0°, implying that the electrode impedance became increasingly resistive. In particular, the impedance of the MoS_2 electrodes was inversely proportional to the density of the nanowells at a biologically relevant frequency of 1 kHz, and the optimum value of 217 $M\Omega\ \mu m^2$, which was about 2.4 times lower than that of bare electrodes, was reached (Figure 2E). The decrement in impedance was attributed to the formation of numerous nanowells on the electrode surface. These nanowells could store charge, ensure the expansion of the activation area for sensitive reaction sites, and enhance charge storage and transfer capabilities without increasing the electrode geometry.

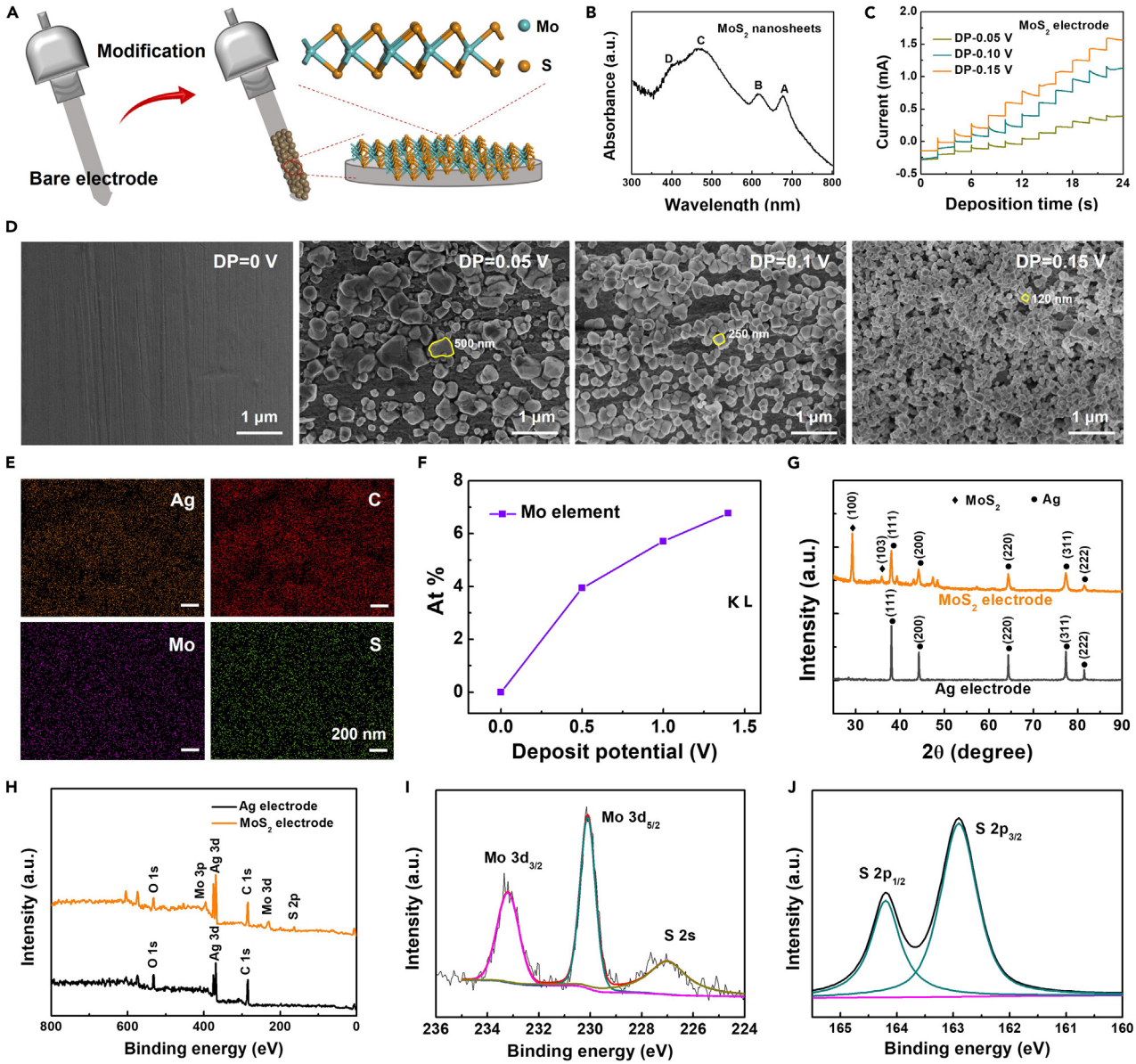

Figure 1. Surface topography and structural characterization of MoS_2 electrodes

(A) Schematic diagram of MoS_2 electrodes.

(B) UV-vis absorption spectra of MoS_2 nanosheets.

(C) Response current of MoS_2 electrodes at different deposition potentials of 0.05 V, 0.10 V and 0.15 V.

(D) The representative SEM images of MoS_2 electrodes at different deposition potentials.

(E) The corresponding EDX elemental mapping images of MoS_2 electrodes.

(F) The content of Mo element increases linearly with the deposition potentials in MoS_2 electrodes.

(G) XRD patterns of MoS_2 electrodes.

(H) XPS survey spectrum of MoS_2 electrodes.

(I and J) XPS high-resolution scan of (I) Mo 3d and (J) S 2p of MoS_2 electrodes.

The electrochemical impedance spectroscopy data were fitted to an equivalent circuit model (inset of Figure 2F) to thoroughly understand the electrochemical performance of the MoS_2 electrodes, and the fitting results are shown in Table S1. The high-frequency regions of the Nyquist plot were composed of a single capacitive reactance arc, indicating that the MoS_2 electrodes were controlled by the charge transfer process. The inset shows the equivalent circuit model for a typical electrode. Charge transfer resistance (R_{ct}) was employed to evaluate the electron transport capabilities, which are typically quantified by the diameter of the semicircle in the Nyquist plot. The results revealed that R_{ct} was progressively enhanced by the increasing nanowell density of the MoS_2 electrodes because the nanowells formed on the surface of the

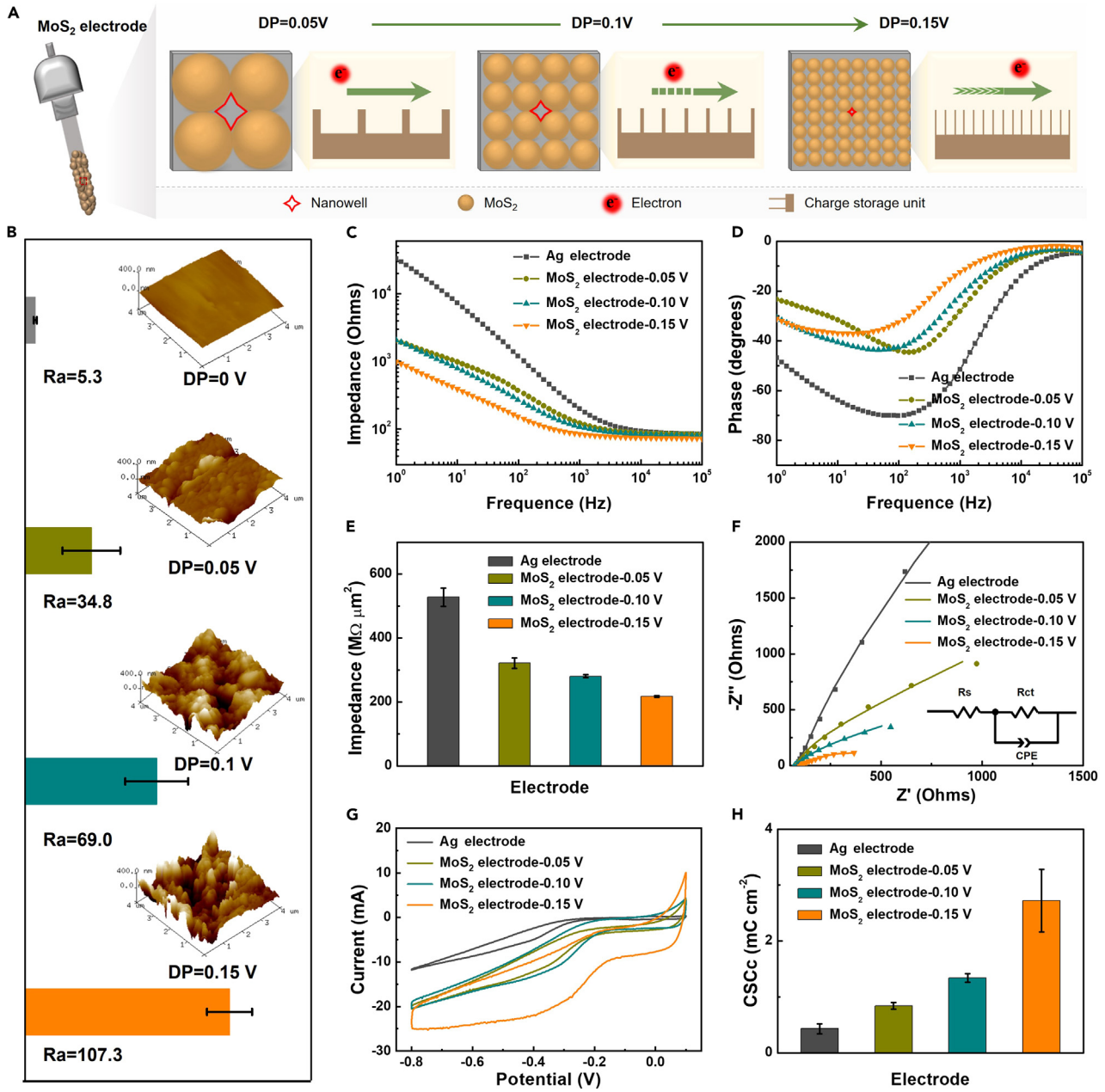

Figure 2. The electrochemical performance of MoS_2 electrodes

(A) Schematic drawing of the nanowell structure of MoS_2 electrodes.

(B) Surface roughness of MoS_2 electrodes at deposition potentials of 0 V, 0.05 V, 0.1 V, and 0.15 V. Error bars show SD. Inset: 3D surface morphology of MoS_2 electrodes.

(C and D) The Bode plot of (C) magnitude and (D) phase of electrodes as a function of the frequency with different deposition potentials.

(E) The specific impedance of electrodes at 1 kHz. Error bars show SD.

(F) The Nyquist plot of MoS_2 electrodes. Inset, the equivalent circuit model for MoS_2 electrodes. R_s is the solution resistance, R_{ct} is the charge transfer resistance, CPE is the constant phase element between the electrode and the PBS solution.

(G and H) (G) CV, and (H) CSCc comparison of different deposition potentials of MoS_2 electrodes. Error bars show SD.

MoS_2 electrodes provided a high-speed path for charge transfer and promoted interfacial charge transfer. For the nonlinear constant phase element (CPE), a small CPE-n indicated that the MoS_2 electrodes possessed a high kinetic velocity of the electrochemical reaction, and a large CPE-Q indicated low impedance and high efficiency in current conduction. For the neural recording electrodes, a large interfacial capacitance was favorable for the suppression of electronic noise, which can be further studied via *in vivo* neural recording. CSCc was used to characterize

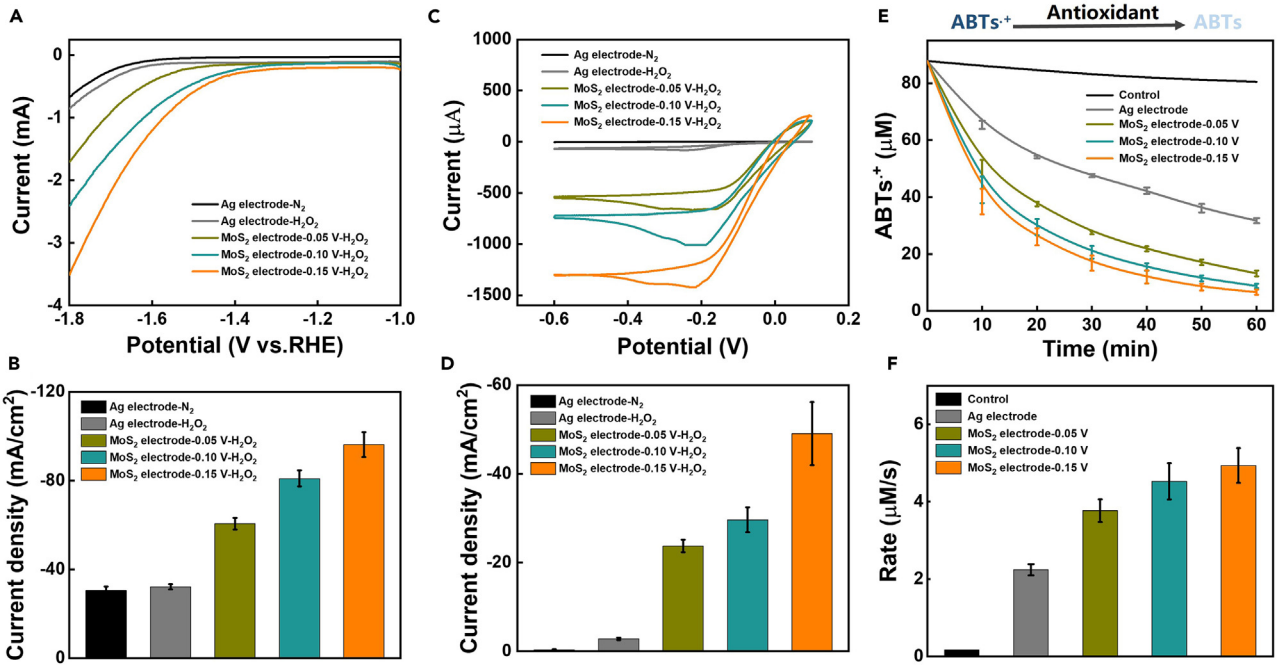

Figure 3. Electrocatalytic and antioxidant activities of MoS_2 electrodes

(A) Polarization curves of MoS_2 electrodes with different deposition potentials in the absence and presence of 10.00 mM H_2O_2 in N_2-saturated 0.01 M PBS.

(B) The current density at an overpotential of −1.8 V for different deposition potentials of the MoS_2 electrode. Error bars show SD.

(C) CVs of MoS_2 electrodes with different deposition potentials in the absence and presence of 10.00 mM H_2O_2 in N_2-saturated 0.01 M PBS.

(D) The negative reduction current response of MoS_2 electrodes at −0.6 V. Error bars show SD.

(E) Deposition potential dependent and time-dependent investigation of $ABTS^{\bullet+}$ for MoS_2 electrodes. Error bars show SD.

(F) The maximum total antioxidant reaction rate of MoS_2 electrodes with increasing deposition potential. Error bars show SD.

the amount of charge that could be injected or transferred using only reversible processes; it is another classic parameter in the field of neural electrodes. The integral area of cathode current in the cyclic voltammetry (CV) curve is defined as CSCc, which represents the ability to store charge. Figures 2G and 2H show that the enclosed area of the MoS_2 electrodes was larger than that of the bare electrodes. CSCc continuously increased with increasing nanowell density until it reached the maximum of 6.9 mC. Therefore, the introduction of MoS_2 considerably enhanced charge transport, and the transferred charge was nearly 6.3 times that of the bare electrodes. Table S2 presents the performance of the MoS_2 electrodes in comparison with that of currently used metallic electrodes and promising modified electrodes. The MoS_2 electrodes, with their biocatalytic activity and enhanced interfacial transport, successfully balanced and fulfilled all the performance aspects, such as high detection sensitivity, excellent stability, and biocompatibility, required for neural electrodes. These aspects are crucial for future clinical translation.

The electrocatalytic activity of electrodes refers to the ability to facilitate a reaction, and it directly affects the efficiency and performance of the electrochemical reaction. The electrocatalytic performance of the MoS_2 electrodes for H_2O_2 was evaluated *in vitro* by linear sweep voltammetry (LSV) and CV. The LSV results showed that the MoS_2 electrodes exhibited a considerably enhanced electrocatalytic reduction, and the current density at an overpotential of −1.8 V was enhanced stepwise by the increasing nanowell density, indicating a high-electrochemical reaction rate (Figures 3A and 3B). When the nanowell density was maximized with the smallest size possible, the current response of the MoS_2 electrodes was 3.2 times higher than that of the bare electrodes and was conducive to improving detection sensitivity. As shown in Figure 3C, the presence of H_2O_2 increased the negative current of CV compared with that in the bare electrodes in the N_2-saturated 1x phosphate buffered saline (PBS) electrolyte, indicating that the MoS_2 electrodes could considerably enhance the catalytic activity of H_2O_2. The negative reduction current response of the MoS_2 electrodes was increased remarkably and positively correlated with nanowell density, and a response enhancement of up to 17.7 times was obtained and contributed to the high electron transfer performance (Figure 3D). The addition of MoS_2 accelerated the catalytic reaction process, indicating that the MoS_2 electrodes had strong catalytic activity, which was attributed to the outstanding electrocatalytic activity of the MoS_2 nanosheets. The MoS_2 nanosheets grown on the surface of the Ag electrodes reconstructed the interfacial structure of the electrode and formed many tiny nanowells, which provided additional reaction sites and helped improve noise suppression. The surface electrons of the MoS_2 electrodes transferred rapidly between the electrode and electrolyte, which prompted the reaction to proceed efficiently and thus enhanced the response sensitivity of the electrode.

Implanting electrodes into brain tissue may trigger oxidative stress, leading to the generation of harmful factors, such as reactive oxygen species, which may have toxic side effects on surrounding biological tissues. MoS_2 nanosheets have excellent antioxidant activity and have

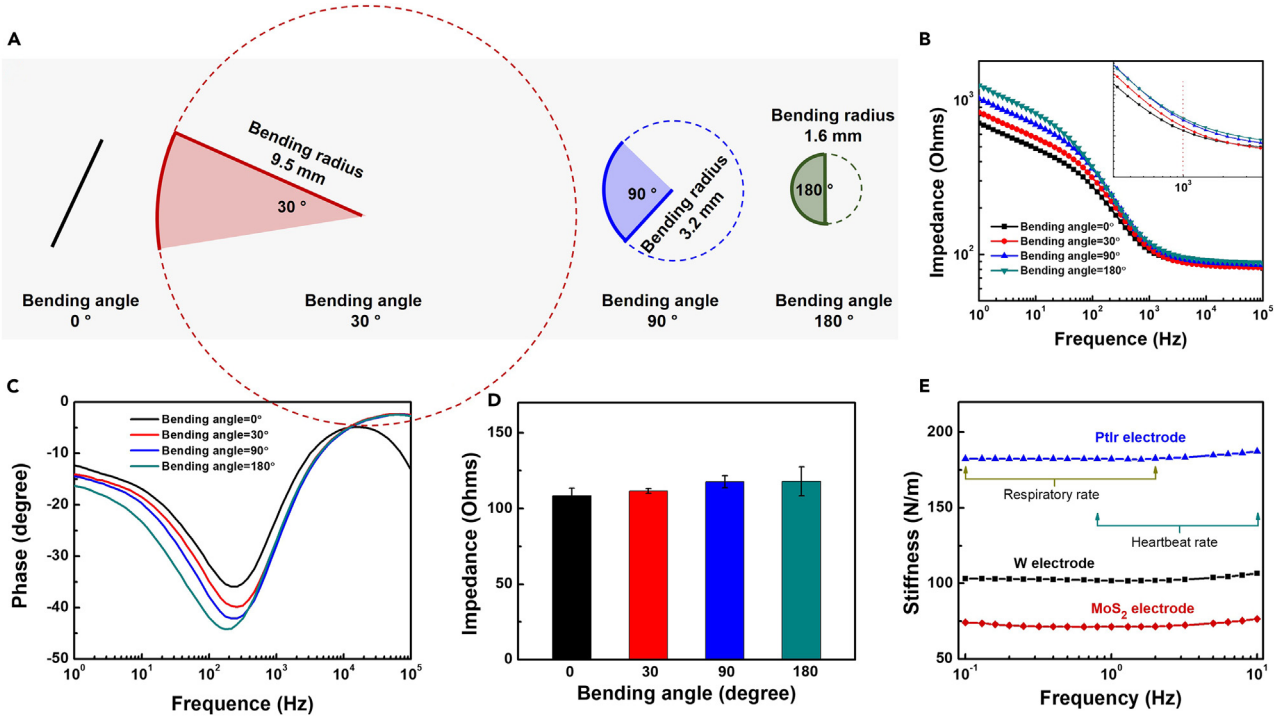

Figure 4. Mechanical properties and bending stiffness of MoS_2 electrodes

(A) Schematic diagram of MoS_2 electrodes with different bending radius.

(B and C) The Bode plot of (B) magnitude and (C) phase of MoS_2 electrodes as a function of the frequency with different bending radius.

(D) The impedance of MoS_2 electrodes in different bending radius at 1 kHz. Error bars show SD.

(E) Comparison of bending stiffness between MoS_2 electrode and clinical PtIr electrode.

been proven to eliminate various free radicals, including hydroxyl radicals (–OH) and nitric oxide ($^{\bullet}$NO), thereby modulating oxidative stress.[41] The total antioxidant activity of the MoS_2 electrodes was determined through the total antioxidant activity test (the 2,2′-azinobis(3-ethylbenzothiaziline-6-sulfonate) rapid method), and the results revealed that the MoS_2 electrodes could achieve a rapid reaction with the substrate at a high reaction rate (Figure 3E). Moreover, a positive correlation was observed between antioxidant capability and nanowell density. Further quantification of the reaction rate indicated that the total antioxidant rate of the MoS_2 electrodes reached 4.9 μM/s at the maximum nanowell density, showing a 2.2-fold increase compared with the total antioxidant rate of the bare electrodes (Figure 3F). The considerably enhanced antioxidant activity of the MoS_2 electrodes was beneficial for reducing the inflammatory damage to brain tissues by effectively scavenging free radicals and improving biocompatibility and long-term neural recording quality.

Interface stability and *in vivo* sensitive neural recording of the MoS_2 electrodes

The stable interface between the nanowell coating and substrate is important in the application of modified electrodes. The mechanical and long-term stabilities of the MoS_2 electrodes were evaluated after 10 min of continuous ultrasound oscillation in PBS to remove the loosening particles and 2 weeks of immersion, respectively. As shown in Figure S4, the impedance of the MoS_2 electrodes at 1 kHz exhibited almost no degradation after ultrasonic treatment for 10 min and soaking for 2 weeks. The SEM images after ultrasonic treatment and immersion revealed that the surface of the MoS_2 electrodes did not exhibit adverse phenomena, such as cracking, exfoliation, and agglomeration, and still showed uniform nanowell structures, suggesting high adhesion and excellent stability (Figures 1D and S5). Inductively coupled plasma-mass spectrometry tests were performed on the immersion solution to quantify the dissolution of the MoS_2 functional layer after ultrasonication and immersion. The results showed that the content of Mo^{4+} was only 0.00072 ± 0.00065 mg/L (Figure S6), which may be due to the strong bonding between the substrate and nanostructured MoS_2 film that resulted in a robust film that could not be easily peeled off even after ultrasonication. The electrode functions under different bending radii were characterized at bending angles of 30°, 90°, and 180° to further verify the mechanical properties of the MoS_2 electrodes (Figure 4A). The results showed that impedance was attenuated by only 8.8% even when the MoS_2 electrodes were under considerable deformation (180° bending), during which the electrodes could still maintain excellent electric performance (Figures 4B–4D). Furthermore, bending stiffness was more relevant than the elastic modulus in the case of tissue micromotion because the electrodes were fixed to the skull after implantation into the brain tissue and were not expected to experience compressive or tensile stress.[42] We therefore conducted complementary tests on the bending stiffness of the MoS_2 electrodes by using a dynamic mechanical analyzer with a double cantilever clamp. The tests were performed over a range of animal respiratory and

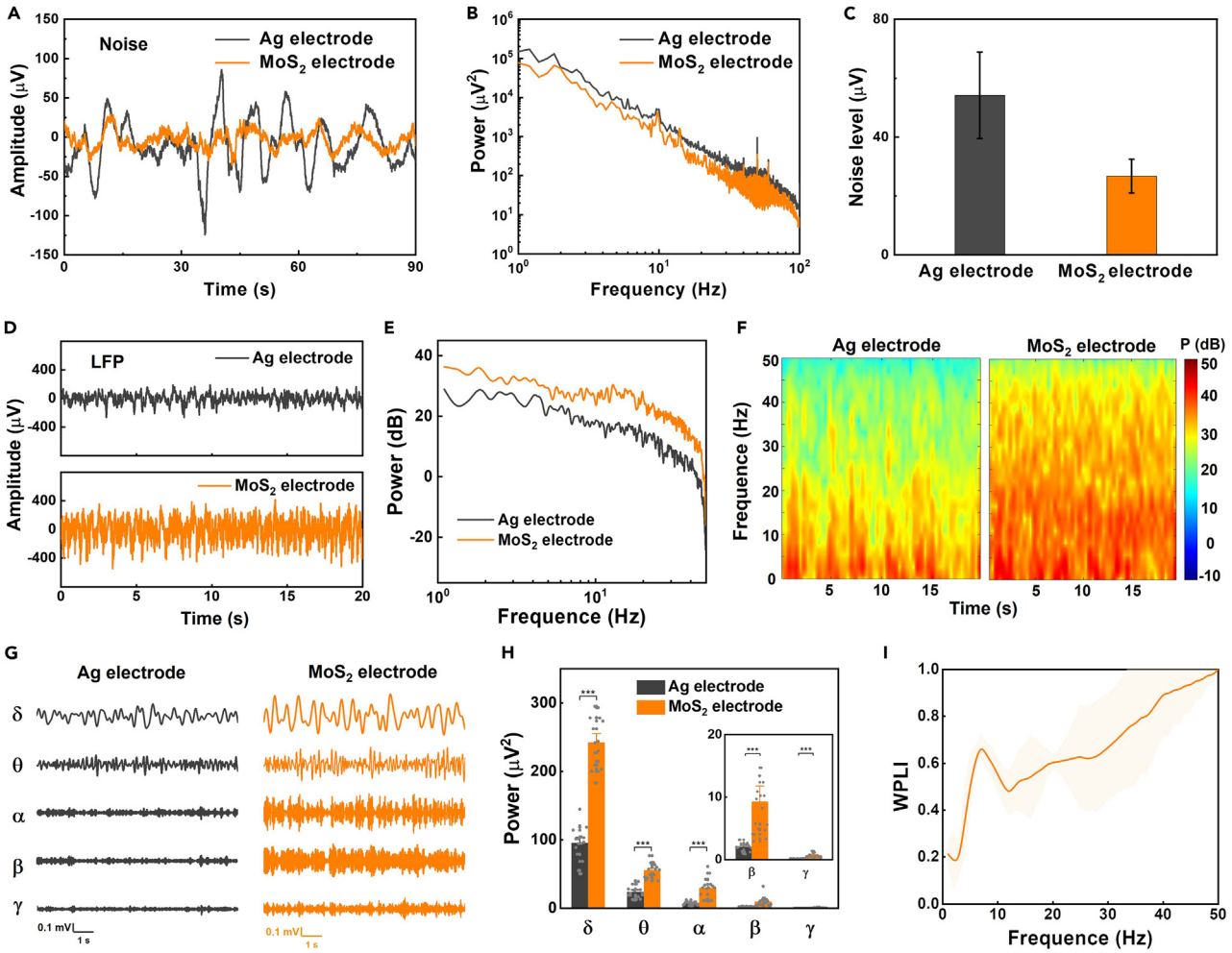

Figure 5. *In vivo* recording quality of MoS_2 electrodes

(A) The time-domain diagram of noise level for MoS_2 electrodes.

(B) Corresponding noise power spectra through FFT for the MoS_2 electrodes.

(C) The noise level amplitude analysis of MoS_2 electrodes. Error bars show SD. (D) The time-domain diagram of LFP signal.

(E and F) The power spectra (E) and time-frequency spectral analysis (F) of MoS_2 electrodes.

(G and H) The comparison of time-domain signal (G) and power analysis (H) in various rhythms of MoS_2 electrodes, including δ, θ, α, β, γ. Error bars show SD. $n = 6$. Gray points are data distributions. ***$p < 0.001$.

(I) WPLI results of MoS_2 electrode signal versus Ag electrode signal as a function of frequency. Shadows show SD.

heartbeat values (0.1–10 Hz) under a controlled displacement of 100 μm. As shown in Figures S7 and 4E, the bending stiffness of the MoS_2 electrodes was similar to that of the bare electrodes at 60–80 N/m and considerably lower than that of comparably sized W and clinical PtIr electrodes commonly used in electrophysiological recordings, which is why MoS_2 electrodes cause minimal damage in the presence of tissue micromotion during chronic studies.

A low noise interference during bioelectrical signal recording allows for the efficient and accurate monitoring of brain activity and provides high sensitivity for diagnosing neurological disorders. Background noise associated with neural electrodes mainly consists of thermal and environmental noises introduced by the system, which largely depend on the impedance of the components in the input circuit. We simultaneously immersed MoS_2 and bare electrodes in artificial cerebrospinal fluid to simulate the tissue fluid microenvironment, and the noise level of the electrodes was recorded without any neural signal input. As shown in Figure 5A, the bare electrodes had obvious noise burrs, and the noise baseline dropped rapidly after MoS_2 modification, indicating that the formation of tiny nanowells and the improved electrocatalytic activity exerted a remarkable influence on the noise level, resulting in a considerable difference in noise between the electrodes. As shown in Figure 5B, the noise trace of 90 s was transformed to the frequency domain by fast Fourier transform, and the results revealed that the MoS_2 electrodes with a high nanowell density had low average noise power in the frequency range of 1–100 Hz. Further comparison of the noise peak-to-peak voltage indicated that the noise level recorded by the bare electrodes was 54.2 μV. Under the same environment and

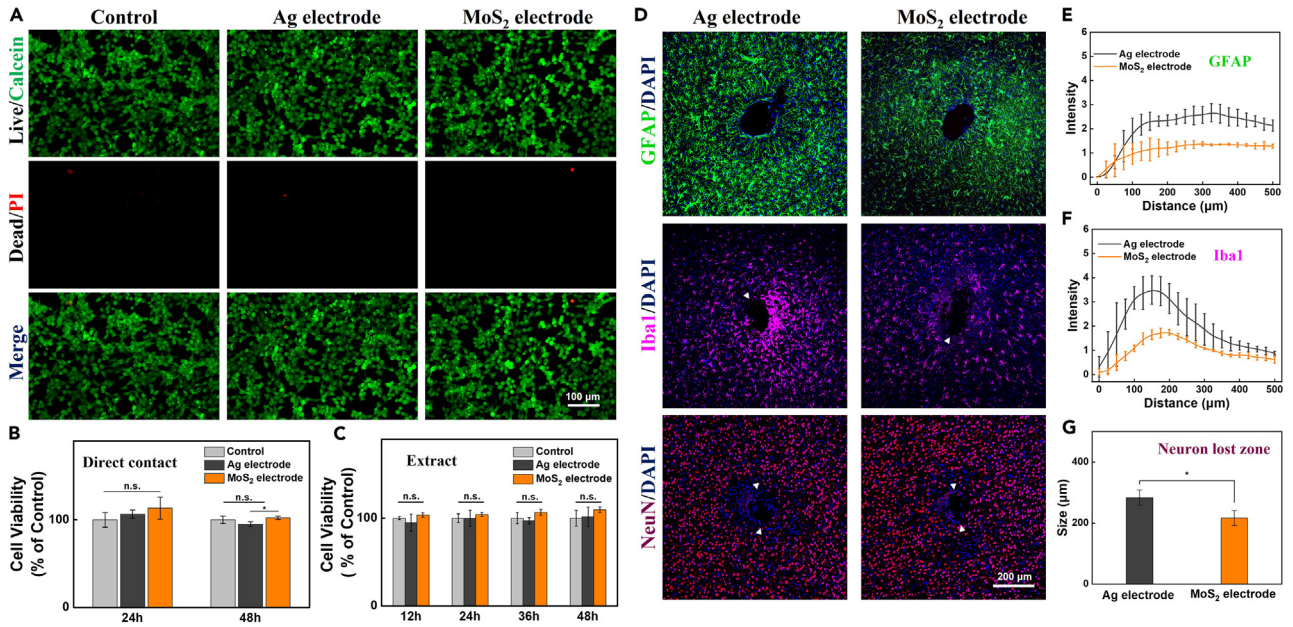

Figure 6. *In vitro* cytotoxicity test and *in vivo* histological studies of tissue response to implanted MoS_2 electrodes

(A) Representative fluorescence images of live/dead HT22 cells after 48 h of direct contact with Ag electrodes and MoS_2 electrodes.

(B) Cell viability of HT22 cells in direct contact with electrodes. $n = 5$ per group. Error bars show SD. n.s.: not significant.

(C) Normalized Cell viability of HT22 cells cultured with extracts of Ag and MoS_2 electrodes at different times was measured by CCK-8 assay. $n = 5$ per group. Error bars show SD. n.s.: not significant. $^*p < 0.05$.

(D–G) Representative fluorescence images of tissue responses 1 week after implantation of Ag electrodes and MoS_2 electrodes, both with a diameter of 200 μm and implanted contralaterally in the same rat. The tissue cells are marked as astrocytes (green), microglia (purple), neuronal cells (red), and nuclei (blue). The fluorescence images undergo normalized fluorescence intensity quantitative analysis for astrocytes (E), microglia (F), and the size of the neuron lost zone (G). Error bars show SD. $n = 6$. $^*p < 0.05$.

experimental conditions, the MoS_2 electrodes with a maximized nanowell density could monitor a low noise level of 26.8 μV, which was two times lower than that of the unmodified electrodes (Figure 5C). The bare and MoS_2 electrodes were implanted into the symmetrical CA3 brain region of rats to monitor *in vivo* neural signals. As shown in Figure 5D, the MoS_2 electrodes detected LFP activity with a high oscillation amplitude, resulting in high detection sensitivity. The power spectral density and time-frequency analysis results indicated that the MoS_2 electrodes exhibited high power values after band-pass filtering in the 1–50 Hz range, suggesting strong signal recording capabilities across the entire LFP frequency band (Figures 5E and 5F). As presented in Figures 5G and 5H, the time-domain waveform under different frequency bands and power spectra further proved that the signal intensity increased by multiples in δ, θ, α, β, and γ rhythm, with a maximum increase of 4.7 times. In the multiple *in vivo* electrophysiologic signal recording experiments ($n = 6$), the electrophysiologic signal results exhibited a high degree of uniformity. As shown in Figures S8–S12, the oscillation amplitude of the signal recorded by the MoS_2 electrodes was stronger than the oscillation amplitude of the signal recorded by the Ag electrodes. The MoS_2 electrodes had high signal energy because of their low impedance, which reduced the energy loss during signal transmission and captured the weak signal. The good noise suppression ability exhibited by the MoS_2 electrodes in the multiple repetitive experiments revealed that the MoS_2 electrodes had excellent reproducibility and sensitivity.

The weighted phase lag index (WPLI) for the two-channel signals was calculated to determine if the LFPs acquired by the MoS_2 and bare electrodes were homologous signals.[43] The random signal matching experiment revealed that the WPLIs of the non-time-synchronized signals were below 0.5 (Figure S13), indicating the high phase synchronization between two segments of the electrophysiological signals identified at WPLI greater than 0.5. The WPLIs of the time-synchronized electrophysiological signals were greater than 0.5 in the frequency range of 10–50 Hz (Figure 5I), indicating strong phase synchronization between the dual-channel signals, which provided evidence of their homology. In short, the many tiny nanowells on the MoS_2 electrodes increased the number of effective reaction sites, thereby reducing the electrode recording impedance and increasing the noise suppression rate. Improving the sensitivity of MoS_2 electrodes allows for the detection of weak neural signals and provides abundant signal information for research on brain function neural decoding and regulation. MoS_2 electrodes are expected to become new candidates in neural recording.

In vitro cytotoxicity and *in vivo* tissue staining assays were conducted to assess the biocompatibility of the MoS2 electrodes (Figure 6). The *in vitro* cytotoxicity of the electrodes was evaluated using the HT22 cell line, Cell Counting Kit-8 (CCK-8), and Calcein/PI Cell Viability/Cytotoxicity Assay Kit. The results of the 24 and 48 h incubations showed that the surviving HT22 cells uniformly and densely adhered to the bottom of the well plates, and the bare and MoS_2 electrodes exhibited good cytocompatibility during direct contact with the HT22 cells (Figures 6A and S14). Quantitative analysis and normalization of the fluorescence images for cell activity revealed that the cell survival rate of the

MoS_2 electrodes exceeded 100% when compared with that of the control group, and the survival rate was maximally increased by 7.6% relative to that of the bare electrodes (Figure 6B). Afterward, bare and MoS_2 electrodes with the same size were immersed in equal volumes of a cell-culture medium and incubated in a cell-culture incubator for 24 h. The extracts were added to 96-well plates seeded with HT22 cells at a uniform density and incubated for 12, 24, 36, and 48 h. The CCK-8 solution was added, incubation was performed for 1 h, and the absorbance of the supernatant was measured. As shown in Figure 6C, the average cell survival rates of the bare and MoS_2 electrodes exceeded 90% and 100%, respectively, indicating that both types of electrodes were free of soluble cytotoxic factors. We further assessed the *in vivo* biocompatibility of the MoS_2 electrodes one week after implantation via histology studies. As shown in Figures 6D and S15, tissue sections were stained via immunohistochemistry for selected markers to visualize the presence of neuronal nuclei (NeuN), astrocytes (GFAP), microglia (Iba1), and cell nuclei (DAPI). The accumulation of activated microglia and astrocytes, together with the neuronal loss around the electrode-tissue interface, is characteristic of brain tissue inflammatory response to implanted electrodes. For the MoS_2 electrodes, an increase was observed in the number of $GFAP^+$ and $Iba1^+$ cells compared with the background tissue at the vicinity of the implant site, and this increment occurred concurrently with a moderate decrease in the number of $NeuN^+$ cells. As shown in Figures 6E and 6F, a 2-fold reduction was observed in the accumulation of astrocytes and expression of general microglia around the MoS_2 electrodes relative to the bare electrodes, indicating an overall reduction in the extent of gliosis, which may be attributed to the high biocatalytic activity of MoS_2. The neuron lost zone, defined as the area around the implants with considerably lowered neuron density, was slightly larger in the MoS_2 electrodes than in the implant footprint and was reduced by a factor of 1.3 compared with that in the Ag electrode (Figure 6G). This trend was also seen in the results of co-staining of NeuN and GFAP (Figure S15). These results indicate that the MoS_2 electrodes exerted negligible toxicity on the brain tissues and had good biocompatibility and biosafety.

DISCUSSION

Compelling evidence indicates that emerging nanotechnology enhances the electrical performance and neural recording efficiency of implanted electrodes. Nanomaterials, such as PEDOT,[44] nanoenzymes,[26] graphene,[16,45] and carbon nanotubes,[46] characterized by excellent electronic conductivity have emerged as promising electrode candidate materials in the past decade. Electron transfer efficiency is considerably enhanced by modifying the electrode surface, thereby augmenting the sensitivity and efficiency of electrode recordings. Although current achievements are encouraging, the weak adhesion of nanocoatings to substrates poses a challenge to long-term implantation and makes nanocoatings prone to detachment or delamination. Enhancing structural and functional durability remains a formidable challenge in clinical translation. In this work, we developed quantized 2D MoS_2 electrodes with strong adhesion by incorporating bioactive MoS_2 nanosheets with excellent catalytic activity and carrier mobility onto the surface of bare electrodes to achieve sensitive neural recording by lowering the interfacial electron transport barriers. 2D MoS_2 nanosheets have exceptional electrical conductivity and electrocatalytic activity, rendering them ideal electrode materials. These nanosheets, characterized by a high surface area, increase the contact interface between the electrode and neurons, thus providing numerous reaction sites and enhancing signal conduction efficiency. MoS_2 nanosheets also manifest a certain level of chargeability and have potential applications in modulating neuronal activity and augmenting the interaction between electrodes and neural tissues. Although the electrical performance of MoS_2 electrodes is slightly inferior to that of the currently best-performing PEDOT, namely, PSS-modified and Pt-black-modified electrodes (Table S2), their primary advantage is that they enhance interfacial electron transfer and biological activity, achieving balance among signal quality, biocompatibility, and stability.

With the rapid development of Moiré materials and related van der Waals heterostructures, the electron transfer efficiency of neural electrodes has room for substantial improvement.[47] MoS_2 nanosheets grown on the surface of traditional electrodes exhibit increasingly uniform sizes with high deposition potentials. This formation creates numerous tiny nanowells that can store charge, provide a high-speed pathway for charge transfer, and promote interface charge transfer. The impedance and CSCc of MoS_2 electrodes are considerably enhanced by the increased effective reaction sites on the surface, which contribute to noise reduction and SNR improvement in neural recordings. The introduction of MoS_2 remarkably enhances the electrocatalytic activity of the electrode, facilitating an efficient current transmission and improving the electrode's response sensitivity. Simultaneously, it helps decrease immune responses and diminish the potential for foreign body reactions. Enhanced sensitivity in the signal recording of MoS_2 electrodes facilitates the precise localization of epileptic foci, aids in surgical navigation, and guides the intraoperative resection of epileptic lesions while preserving vital functional areas, thereby avoiding postoperative neurofunctional deficits. Furthermore, neural electrodes based on 2D MoS_2 materials can be extended to deep brain stimulation, enabling a precise modulation of neurological disorders. Additionally, the use of cutting-edge complementary metal-oxide semiconductor (CMOS) manufacturing techniques can transform these 2D material-based needle electrodes into high-density electrode arrays, allowing for the detection of globally coordinated brain regions and achieving highly sensitive, high-throughput recordings. Versatile MoS_2 electrodes are essential for future neuroscience research and clinical applications.

In summary, we developed an implantable neural electrode with a nanowell structure for improved neural recording quality by growing MoS_2 nanosheets on the surface of a Ag electrode. 2D MoS_2 nanosheets have excellent catalytic activity and carrier mobility, and their introduction onto the electrode surface in this study created numerous tiny nanowells that could store charge. The impedance and CSCc of the MoS_2 electrodes improved gradually with the increase in nanowell density and reached 217 $M\Omega\ \mu m^2$ and 6.9 mC, respectively. The catalytic activity of the MoS_2 electrodes increased by 17.7-folds, which prompted the reaction to proceed efficiently and enhanced the response sensitivity of the electrode. *In vivo* and *in vitro* experiments demonstrated that the MoS_2 electrodes had high biosafety and biocompatibility. The MoS_2 electrodes exhibited enhanced sensitivity in recording LFP activities because of the quantized charge storage units and improved electrical properties, potentially enabling highly efficient neural recordings. This work can serve as a guide in the sensitive, accurate diagnosis of neurological disorders.

Limitations of the study

The modification of electrodes with nanomaterials to improve electrical performance and sensitivity is a common method. Generally, Ag is not used in invasive *in vivo* applications because of its cytotoxicity.[48] In this study, given the ultra-high conductivity, low cost, and easy modification of Ag, highly bioactive MoS_2 nanosheets were introduced onto the surface of a Ag electrode to enhance electrode performance. MoS_2 was uniformly distributed on the Ag surface, which hindered the direct contact of Ag with brain tissue and prevented *in vivo* toxicity. Although many current nanomaterials have good biocompatibility *in vitro*, their biocompatibility and stability in long-term implantation *in vivo* remain problematic. Future research could consider optimization on substrates, such as stable Pt, PtIr, Au, and extensively studied graphene fibers, and design advanced bio-nanomaterials as the electrode functional layer for the development of efficient and compatible electrodes with many biomimetic interfaces, further blurring the boundaries between electrodes and biological tissues. In addition, future research could apply state-of-the-art CMOS techniques to transform needle electrodes into high-density and ECoG electrode arrays for probing globally coordinated brain regions for sensitive brain-machine interfaces and high-throughput recording.

RESOURCE AVAILABILITY

Lead contact

Further information and requests for resources and reagents should be directed to and will be fulfilled by the Lead Contact, Xiao-Dong Zhang (xiaodongzhang@tju.edu.cn).

Materials availability

This study did not generate new unique reagents.

Data and code availability

- Any data required to reanalyze the data reported in this paper are available from the lead contact upon request.
- All data reported in this paper will be shared by the lead contact upon request.
- This paper does not report original code.
- Any additional information required to reanalyze the data reported in this paper is available from the lead contact upon request.

ACKNOWLEDGMENTS

This work was financially supported by the National Key Research and Development Program of China (2021YFF1200700), the National Natural Science Foundation of China (grant nos. 91859101, 81971744, U1932107, 82001952, 11804248, 82302361, and 82302381), Outstanding Youth Funds of Tianjin (2021FJ-0009), STI 2030—Major Projects (2022ZD0210200), National Natural Science Foundation of Tianjin (nos. 19JCZDJC34000, 20JCYBJC00940, 21JCYBJC00550, 21JCZDJC00620, and 21JCYBJC00490), the Innovation Foundation of Tianjin University, China Postdoctoral Science Foundation (2023M732601) and CAS Interdisciplinary Innovation Team (JCTD-2020-08).

AUTHOR CONTRIBUTIONS

S.L., X.-D.Z., and D.M. conceived and designed the experiments. S.L., X.S., and Y.W. contributed to electrophysiological experiment, X.S., K.L., and R.L. contributed to materials synthesis, S.L., X.S., Y.Z., Z.N., and W.T. contributed to characterization and electrochemical measurement; S.L. and X.S. analyzed the data; S.L., X.S., S.Z., X.M., H.W., X.-D.Z., and D.M. prepared the manuscript. All authors discussed the results and commented on the manuscript.

DECLARATION OF INTERESTS

The authors declare no competing interests.

STAR★METHODS

Detailed methods are provided in the online version of this paper and include the following:

SUPPLEMENTAL INFORMATION

Supplemental information can be found online at https://doi.org/10.1016/j.isci.2024.110949.

Received: January 27, 2024
Revised: May 6, 2024
Accepted: September 10, 2024
Published: September 13, 2024

REFERENCES

1. Hong, G., and Lieber, C.M. (2019). Novel electrode technologies for neural recordings. Nat. Rev. Neurosci. *20*, 330–345. https://doi.org/10.1038/s41583-019-0140-6.
2. Liu, T.C., Chuang, M.C., Chu, C.Y., Huang, W.C., Lai, H.Y., Wang, C.T., Chu, W.L., Chen, S.Y., and Chen, Y.Y. (2016). Implantable Graphene-based Neural Electrode Interfaces for Electrophysiology and Neurochemistry in In Vivo Hyperacute Stroke Model. ACS Appl. Mater. Inter. *8*, 187–196. https://doi.org/10.1021/acsami.5b08327.
3. Buzsaki, G., Anastassiou, C.A., and Koch, C. (2012). The origin of extracellular fields and currents–EEG, ECoG, LFP and spikes. Nat. Rev. Neurosci. *13*, 407–420. https://doi.org/10.1038/nrn3241.
4. Chen, R., Canales, A., and Anikeeva, P. (2017). Neural Recording and Modulation Technologies. Nat. Rev. Mater. *2*, 16093. https://doi.org/10.1038/natrevmats.2016.93.
5. Tybrandt, K., Khodagholy, D., Dielacher, B., Stauffer, F., Renz, A.F., Buzsáki, G., and Vörös, J. (2018). High-Density Stretchable Electrode Grids for Chronic Neural Recording. Adv. Mater. *30*, e1706520. https://doi.org/10.1002/adma.201706520.
6. Zhao, Y., Zhang, S., Yu, T., Zhang, Y., Ye, G., Cui, H., He, C., Jiang, W., Zhai, Y., Lu, C., et al. (2021). Ultra-conformal skin electrodes with synergistically enhanced conductivity for long-time and low-motion artifact epidermal electrophysiology. Nat. Commun. *12*, 4880. https://doi.org/10.1038/s41467-021-25152-y.
7. Liu, J., Li, F., Wang, Y., Pan, L., Lin, P., Zhang, B., Zheng, Y., Xu, Y., Liao, H., Ko, G., et al. (2020). A sensitive and specific nanosensor for monitoring extracellular potassium levels in the brain. Nat. Nanotechnol. *15*, 321–330. https://doi.org/10.1038/s41565-020-0634-4.
8. Wang, C., Sun, W., Zhang, J., Zhang, J., Guo, Q., Zhou, X., Fan, D., Liu, H., Qi, M., Gao, X., et al. (2021). An electric-field-responsive paramagnetic contrast agent enhances the visualization of epileptic foci in mouse models of drug-resistant epilepsy. Nat. Biomed. Eng. *5*, 278–289. https://doi.org/10.1038/s41551-020-00618-4.
9. Liu, Y., Li, J., Song, S., Kang, J., Tsao, Y., Chen, S., Mottini, V., McConnell, K., Xu, W., Zheng, Y.Q., et al. (2020). Morphing electronics enable neuromodulation in growing tissue. Nat. Biotechnol. *38*, 1031–1036. https://doi.org/10.1038/s41587-020-0495-2.
10. Xie, K., Zhang, S., Dong, S., Li, S., Yu, C., Xu, K., Chen, W., Guo, W., Luo, J., and Wu, Z. (2017). Portable wireless electrocorticography system with a flexible microelectrodes array for epilepsy treatment. Sci. Rep. *7*, 7808. https://doi.org/10.1038/s41598-017-07823-3.
11. Robinson, D.A. (1968). The electrical properties of metal microelectrodes. Proc. IEEE *56*, 1065–1071. https://doi.org/10.1109/PROC.1968.6458.
12. Loeb, G.E., Peck, R.A., and Martyniuk, J. (1995). Toward the Ultimate Metal Microelectrode. J Neurosci. Meth. *63*, 175–183. https://doi.org/10.1016/0165-0270(95)00107-7.
13. Seker, E., Berdichevsky, Y., Begley, M.R., Reed, M.L., Staley, K.J., and Yarmush, M.L. (2010). The fabrication of low-impedance nanoporous gold multiple-electrode arrays for neural electrophysiology studies. Nanotechnology *21*, 125504. https://doi.org/10.1088/0957-4484/21/12/125504.
14. Fairfield, J.A. (2018). Nanostructured materials for neural electrical interfaces. Adv. Funct. Mater. *28*, 1701145. https://doi.org/10.1002/adfm.201701145.
15. Liu, S., Zhao, Y., Hao, W., Zhang, X.-D., and Ming, D. (2020). Micro-and nanotechnology for neural electrode-tissue interfaces. Biosens. Bioelectron. *170*, 112645. https://doi.org/10.1016/j.bios.2020.112645.
16. Wang, K., Frewin, C.L., Esrafilzadeh, D., Yu, C., Wang, C., Pancrazio, J.J., Romero-Ortega, M., Jalili, R., and Wallace, G. (2019). High-performance graphene-fiber-based neural recording microelectrodes. Adv. Mater. *31*, 1805867. https://doi.org/10.1002/adma.201805867.
17. Du, Z.J., Kolarcik, C.L., Kozai, T.D.Y., Luebben, S.D., Sapp, S.A., Zheng, X.S., Nabity, J.A., and Cui, X.T. (2017). Ultrasoft microwire neural electrodes improve chronic tissue integration. Acta Biomater. *53*, 46–58. https://doi.org/10.1016/j.actbio.2017.02.010.
18. Salatino, J.W., Ludwig, K.A., Kozai, T.D.Y., and Purcell, E.K. (2017). Glial responses to implanted electrodes in the brain. Nat. Biomed. Eng. *1*, 862–877. https://doi.org/10.1038/s41551-017-0154-1.
19. Young, A.T., Cornwell, N., and Daniele, M.A. (2018). Neuro-Nano Interfaces: Utilizing Nano-Coatings and Nanoparticles to Enable Next-Generation Electrophysiological Recording, Neural Stimulation, and Biochemical Modulation. Adv. Funct. Mater. *28*, 1700239. https://doi.org/10.1002/adfm.201700239.
20. Lycke, R., Kim, R., Zolotavin, P., Montes, J., Sun, Y., Koszeghy, A., Altun, E., Noble, B., Yin, R., He, F., et al. (2023). Low-threshold, high-resolution, chronically stable intracortical microstimulation by ultraflexible electrodes. Cell Rep. *42*, 112554. https://doi.org/10.1016/j.celrep.2023.112554.
21. Chung, T., Wang, J.Q., Wang, J., Cao, B., Li, Y., and Pang, S.W. (2015). Electrode modifications to lower electrode impedance and improve neural signal recording sensitivity. J. Neural. Eng. *12*, 056018. https://doi.org/10.1088/1741-2560/12/5/056018.
22. Zhang, X., Pan, B., Wang, K., Ruan, J., Bao, C., Yang, H., He, R., and Cui, D. (2010). Electrochemical Property and Cell Toxicity of Gold Electrode Modified by Monolayer PAMAM Encapsulated Gold Nanorods. Nano BioMed. ENG. *2*, 182–188. https://doi.org/10.5101/nbe.v2i3.p182-188.
23. Shin, J.H., Kim, G.B., Lee, E.J., An, T., Shin, K., Lee, S.E., Choi, W., Lee, S., Latchoumane, C., Shin, H.S., and Lim, G. (2014). Carbon-Nanotube-Modified Electrodes for Highly Efficient Acute Neural Recording. Adv. Healthc. Mater. *3*, 245–252. https://doi.org/10.1002/adhm.201300183.
24. Cho, Y.U., Lee, J.Y., Jeong, U.J., Park, S.H., Lim, S.L., Kim, K.Y., Jang, J.W., Park, J.H., Kim, H.W., Shin, H., et al. (2022). Ultra-Low Cost, Facile Fabrication of Transparent Neural Electrode Array for Electrocorticography with Photoelectric Artifact-Free Optogenetics. Adv. Funct. Mater. *32*, 2105568. https://doi.org/10.1002/adfm.202105568.
25. Kozai, T.D.Y., Langhals, N.B., Patel, P.R., Deng, X., Zhang, H., Smith, K.L., Lahann, J., Kotov, N.A., and Kipke, D.R. (2012). Ultrasmall implantable composite microelectrodes with bioactive surfaces for chronic neural interfaces. Nat. Mater. *11*, 1065–1073. https://doi.org/10.1038/nmat3468.
26. Liu, S., Wang, Y., Zhao, Y., Liu, L., Sun, S., Zhang, S., Liu, H., Liu, S., Li, Y., Yang, F., et al. (2024). A Nanozyme-Based Electrode for High-Performance Neural Recording. Adv. Mater. *36*, 2304297. https://doi.org/10.1002/adma.202304297.
27. Cui, X.T., and Zhou, D.D. (2007). Poly (3, 4-ethylenedioxythiophene) for chronic neural stimulation. IEEE Trans. Neural Syst. Rehabil. Eng. *15*, 502–508. https://doi.org/10.1109/TNSRE.2007.909811.
28. Kozai, T.D.Y., Catt, K., Du, Z., Na, K., Srivannavit, O., Haque, R.U.M., Seymour, J., Wise, K.D., Yoon, E., and Cui, X.T. (2016). Chronic in vivo evaluation of PEDOT/CNT for stable neural recordings. IEEE Trans. Biomed. Eng. *63*, 111–119. https://doi.org/10.1109/TBME.2015.2445713.
29. Lin, C.M., Lee, Y.T., Yeh, S.R., and Fang, W. (2009). Flexible carbon nanotubes electrode for neural recording. Biosens. Bioelectron. *24*, 2791–2797. https://doi.org/10.1002/adhm.201300183.
30. Zhao, S., Li, G., Tong, C., Chen, W., Wang, P., Dai, J., Fu, X., Xu, Z., Liu, X., Lu, L., et al. (2020). Full activation pattern mapping by simultaneous deep brain stimulation and fMRI with graphene fiber electrodes. Nat. Commun. *11*, 1788. https://doi.org/10.1038/s41467-020-15570-9.
31. Guo, Y., Jiang, S., Grena, B.J.B., Kimbrough, I.F., Thompson, E.G., Fink, Y., Sontheimer, H., Yoshinobu, T., and Jia, X. (2017). Polymer Composite with Carbon Nanofibers Aligned during Thermal Drawing as a Microelectrode for Chronic Neural Interfaces. ACS Nano *11*, 6574–6585. https://doi.org/10.1021/acsnano.6b07550.
32. Lu, L., Fu, X., Liew, Y., Zhang, Y., Zhao, S., Xu, Z., Zhao, J., Li, D., Li, Q., Stanley, G.B., and

Duan, X. (2019). Soft and MRI compatible neural electrodes from carbon nanotube Fibers. Nano Lett. *19*, 1577–1586. https://doi.org/10.1021/acs.nanolett.8b04456.

33. Kuzum, D., Takano, H., Shim, E., Reed, J.C., Juul, H., Richardson, A.G., de Vries, J., Bink, H., Dichter, M.A., Lucas, T.H., et al. (2014). Transparent and flexible low noise graphene electrodes for simultaneous electrophysiology and neuroimaging. Nat. Commun. *5*, 5259. https://doi.org/10.1038/ncomms6259.
34. Radisavljevic, B., Radenovic, A., Brivio, J., Giacometti, V., and Kis, A. (2011). Single-layer MoS2 transistors. Nat. Nanotechnol. *6*, 147–150. https://doi.org/10.1038/nnano.2010.279.
35. Rowley-Neale, S.J., Brownson, D.A.C., Smith, G.C., Sawtell, D.A.G., Kelly, P.J., and Banks, C.E. (2015). 2D nanosheet molybdenum disulphide (MoS_2) modified electrodes explored towards the hydrogen evolution reaction. Nanoscale *7*, 18152–18168. https://doi.org/10.1039/C5NR05164A.
36. You, X., Liu, N., Lee, C.J., and Pak, J.J. (2014). An electrochemical route to MoS_2 nanosheets for device applications. Mater. Lett. *121*, 31–35. https://doi.org/10.1039/c5nr05164a.
37. Wang, Y., Udyavara, S., Neurock, M., and Frisbie, C.D. (2019). Field effect modulation of electrocatalytic hydrogen evolution at back-gated two-dimensional MoS_2 electrodes. Nano Lett. *19*, 6118–6123. https://doi.org/10.1021/acs.nanolett.9b02079.
38. Joseph, N., Shafi, P.M., and Bose, A.C. (2020). Recent advances in 2D-MoS_2 and its composite nanostructures for supercapacitor electrode application. Energy Fuels *34*, 6558–6597. https://doi.org/10.1021/acs.energyfuels.0c00430.
39. Ding, X., Peng, F., Zhou, J., Gong, W., Slaven, G., Loh, K.P., Lim, C.T., and Leong, D.T. (2019). Defect engineered bioactive transition metals dichalcogenides quantum dots. Nat. Commun. *10*, 41. https://doi.org/10.1038/s41467-018-07835-1.
40. Baker, M., Gilmore, R., Lenardi, C., and Gissler, W. (1999). XPS investigation of preferential sputtering of S from MoS_2 and determination of MoS_x stoichiometry from Mo and S peak positions. Appl. Surf. Sci. *150*, 255–262. https://doi.org/10.1016/S0169-4332(99)00253-6.
41. Zhang, X., Zhang, S., Yang, Z., Wang, Z., Tian, X., and Zhou, R. (2021). Self-cascade MoS_2 nanozymes for efficient intracellular antioxidation and hepatic fibrosis therapy. Nanoscale *13*, 12613–12622. https://doi.org/10.1039/D1NR02366G.
42. Canales, A., Jia, X., Froriep, U.P., Koppes, R.A., Tringides, C.M., Selvidge, J., Lu, C., Hou, C., Wei, L., Fink, Y., and Anikeeva, P. (2015). Multifunctional fibers for simultaneous optical, electrical and chemical interrogation of neural circuits in vivo. Nat. Biotechnol. *33*, 277–284. https://doi.org/10.1038/nbt.3093.
43. Vinck, M., Oostenveld, R., Van Wingerden, M., Battaglia, F., and Pennartz, C.M.A. (2011). An improved index of phase-synchronization for electrophysiological data in the presence of volume-conduction, noise and sample-size bias. Neuroimage *55*, 1548–1565. https://doi.org/10.1016/j.neuroimage.2011.01.055.
44. Takashi, D., Langhals, N.B., Patel, P.R., Deng, X., Zhang, H., Smith, K.L., Lahann, J., Kotov, N.A., and Kipke, D.R. (2012). Ultrasmall implantable composite microelectrodes with bioactive surfaces for chronic neural interfaces. Nat. Mater. *11*, 1065–1073. https://doi.org/10.1038/nmat3468.
45. Zhao, S., Li, G., Tong, C., Chen, W., Wang, P., Dai, J., Fu, X., Xu, Z., Liu, X., Lu, L., et al. (2020). Full activation pattern mapping by simultaneous deep brain stimulation and fMRI with graphene fiber electrodes. Nat. Commun. *11*, 1788. https://doi.org/10.1038/s41467-020-15570-9.
46. Lu, L., Fu, X., Liew, Y., Zhang, Y., Zhao, S., Xu, Z., Zhao, J., Li, D., Li, Q., Stanley, G.B., and Duan, X. (2019). Soft and MRI compatible neural electrodes from carbon nanotube fibers. Nano Lett. *19*, 1577–1586. https://doi.org/10.1021/acs.nanolett.8b04456.
47. Andrei, E.Y., Efetov, D.K., Jarillo-Herrero, P., Macdonald, A.H., Mak, K.F., Senthil, T., Tutuc, E., Yazdani, A., and Young, A.F. (2021). The marvels of moiré materials. Nat. Rev. Mater. *6*, 201–206. https://doi.org/10.1038/s41578-021-00284-1.
48. Dymond, A.M., Kaechele, L.E., Jurist, J.M., and Crandall, P.H. (1970). Brain tissue reaction to some chronically implanted metals. J. Neurosurg. *33*, 574–580. https://doi.org/10.3171/jns.1970.33.5.0574.
49. Vitale, F., Summerson, S.R., Aazhang, B., Kemere, C., and Pasquali, M. (2015). Neural stimulation and recording with bidirectional, soft carbon nanotube fiber microelectrodes. ACS Nano *9*, 4465–4474. https://doi.org/10.1021/acsnano.5b01060.

STAR★METHODS

KEY RESOURCES TABLE

REAGENT or RESOURCE	SOURCE	IDENTIFIER
Antibodies		
Anti-GFAP antibody	Abcam	Cat#ab4648 ; RRID; AB_449329
IBA1 antibody	Thermo Fisher Scientific.	Cat#MA5-27726; RRID:AB_2735228
NeuN antibody	Cell Signaling Technology	Cat#94403S; RRID:AB_2904530
CoraLite488-conjugated Donkey Anti-Rabbit IgG(H + L)	Proteintech	Cat#SA00013-6; RRID:AB_2890972
Donkey Anti-Mouse IgG H&L	Abcam	Cat#ab150108; RRID:AB_2732073
Chemicals, peptides, and recombinant proteins		
MoS_2	Aldrich	Cat#1317-33-5
N,N-dimethylformamide	Aladdin	Cat#7087-68-5
Ag wire	Sino-Platinum Metals C0.	N/A
Experimental models: Cell lines		
HT22 cells	Institute of Radiation Medicine, Chinese Academy of Medical Sciences	N/A
Experimental models: Organisms/strains		
Wistar rats (male, 250–280 g)	Beijing Vital River Laboratory Animal Technology	N/A
Other		
Calcein/PI Cell Live/Dead Viability/Cytotoxicity Assay Kit	Beyotime	Cat#C2015S
Cell Counting Kit-8	APExBIO	Cat#K1018

EXPERIMENTAL MODEL AND SUBJECT DETAILS

Ethics statement

All experiments were carried out in accordance with the Animal Management Rules of the Ministry of Health of the People's Republic of China and were reviewed by Animal Ethical and Welfare of Tianjin University (TJUE-2023-141).

Cell culture

HT22 cells were obtained from the Institute of Radiation Medicine, Chinese Academy of Medical Sciences, and used for all *in vitro* cytotoxicity assays. The cell culture medium was Dulbecco's Modified Eagle Medium (DMEM) (Gibco) with 10% fetal bovine serum (FBS, BI). In all, 100 U/mL penicillin and 100 mg/mL streptomycin sulfate (Solomo) were applied according to the growth state.

Direct contact cytotoxicity test

HT22 cells (1×10^5) were cultured in 24-well plates in 1 mL culture medium and incubated in the cell culture incubator (5% CO_2, at 37°C) for 24 h. The electrodes were sterilized and cleaned, and cut into 1-cm electrode segments and placed into the cell culture wells. Cells were stained using Calcein/PI Cell Live/Dead Viability/Cytotoxicity Assay Kit (Beyotime, C2015S) after incubation for 24 and 48 h, in which Calcein Acetoxymethyl Ester (Calcein AM) fluorescently stained live cells (green) and Propidium Iodide (PI) stained dead cells (red). Detailed operations were described in the kit instructions. The distribution of live and dead cells after staining was visualized using fluorescence microscopy.

Indirect contact cytotoxicity test

Bare electrodes and MoS_2 electrodes of identical size were immersed in equal volumes of cell culture medium and placed in the cell culture incubator for 24 h. The extracts were then added to 96-well plates seeded with HT22 cells (3×10^3). After 12, 24, 36, and 48 h of incubation, Cell Counting Kit-8 (CCK-8) (APExBIO, K1018, USA) solution was added and incubated for 1 h, and the absorbance of the supernatant was measured at 450 nm using a spectrophotometer. The control group was subjected to the identical test without any electrodes, and cell viability was normalized.

Animal experiments

Adult male Wistar rats (250–280 g) were housed under standard conditions, with *ad libitum* access to food and water. Before the start of the operation, anesthetize rats using isoflurane (5% for induction, 0.5–1.5% for maintenance). The rat's head was then shaved and fixed on a stereotaxic frame with toothed racks and ear bars, and the scalp was incised with a scalpel to expose the skull and then the cranial window was opened using a cranial drill. The bare electrodes and MoS_2 electrodes were slowly inserted into the hippocampal CA3 area of the symmetrical brain region of the rat (3.5 mm lateral and 2.5 mm posterior to bregma; 2 mm depth from the dura mater) using a stereotactic frame, and two stainless-steel screws were implanted to serve as the grounding electrode and the reference electrode.

METHOD DETAILS

Synthesis of MoS_2 nanosheets

The MoS_2 nanosheets were synthesized according to the previous literature.[39] In detail, MoS_2 powder (Aldrich) was dispersed in N,N-dimethylformamide (DMF) at a concentration of 5 mg/mL and then ultrasonication for 12 h to form a black suspension. The above suspension was centrifuged at 4000 rpm for 30 min by a high-speed centrifuge, and the pale yellow supernatant was collected. After centrifugation again at 12000 rpm for 30 min, the precipitates were redispersed into DMF of the same volume as before centrifugation, and L-cysteine was added to achieve a final concentration of 0.1 mg/mL. The mixture was mixed uniformly and kept still for 24 h of aging at room temperature, and the supernatant was centrifuged again at 12000 rpm for 30 min with the precipitates collected. The product was washed extensively with deionized water and centrifuged at 12000 rpm to remove free cysteine and residual DMF.

Fabrication of the MoS_2 electrode

The preparation of the MoS_2 electrode was carried out electrochemically in a three-electrode configuration using the CHI660E electrochemical workstation (CH Instruments, Shanghai, China) via Multi-Potential Steps method. Before preparation, the Ag wire (200 μm in diameter, 99.99%, Sino-Platinum Metals C0., LTD) used as the working electrode was first physically roughened with 400-grit sandpaper to increase the deposition sites of MoS_2 nanosheets and improve the firmness of the subsequent coating. The MoS_2 prepared above was formulated into the working solution at a concentration of 2 mg/mL with deionized water. The Ag/AgCl electrode, platinum wire, and the roughened Ag electrode were used as the reference, counter, and working electrodes, respectively. As illustrated in Figure S16, the step time of the multi-potential step deposition method is 2 s, totaling 24 s. By incrementally setting the deposition potential at step sizes of 0.05 V, 0.1 V, and 0.15 V, the corresponding deposition currents are obtained as depicted in Figure 1C. The results demonstrate a linear increase with the augmentation of deposition potential. Ultimately, the deposition response currents are constrained within the range of 0.2–2.0 mA, which the MoS_2 film layer on the electrode surface exhibits uniformity and strong adhesion. Then, the modified electrodes were placed under an ultraviolet lamp for low temperature baking to increase the firmness and adhesion of the MoS_2-film. Finally, the prepared MoS_2 electrodes were insulated with polyimide with high dielectric coefficient and excellent biocompatibility, and then the effective sites were exposed using sharp scissors for subsequent experiments.

MoS_2 electrode characterization

UV-vis absorption spectra were measured by using a Shimadzu 3600 double-beam spectrophotometer with QS-grade quartz cuvettes at room temperature. XPS spectra analysis was carried out on the ESCALAB 250 Xi system (Thermo Scientific) with an Al Kα X-ray source operating at 300 W, and the original data were peak-fitted in XPSPEAK41 software. The surface morphologies of MoS_2 electrodes and corresponding EDX element mapping images were characterized by a Hitachi S4800 SEM at an accelerating voltage of 10 kV.

Surface roughness of MoS_2 electrode

In order to study the effect of surface roughness on electrode performance, Ag electrode was modified with different deposition potentials of MoS_2, and the surface roughness of the MoS_2 electrode was tested by AFM (Dimension icon, Bruker) in tapping mode with 4×4 μm scan range. In addition, the surface roughness was processed in NanoScope Analysis software and was typically characterized by domain parameters such as the average roughness (Ra).

Electrochemical characterization of the MoS_2 electrode

All electrochemical measurements were carried out in PBS electrolyte at pH 7.4 at room temperature, completed with a CHI660E electrochemical workstation. The three-electrode configuration was used, with the MoS_2 electrodes as the working electrodes, the Ag/AgCl electrode and Pt wire as the potential referenced and counter electrode.

For EIS, the test frequency range was set to 1 - 10^5 Hz, and an AC signal with a disturbance amplitude of 10 mV was applied to the working electrode under the open circuit potential. EIS was fitted by an equivalent circuit model to obtain R_{ct} and the impedance modulus at the biologically relevant frequency of 1 kHz. The specific impedance was calculated by multiplying the impedance value at 1 kHz by the electrode surface area in the Bode plot. The Nyquist plot was analyzed using the fitting software Zview (Scriber Associates, USA).

The CV was performed by scanning for two cycles at a scan rate of 50 mV/s over a potential range of −0.8 V–0.1 V. The CSCc was calculated by integrating the current overtime in the potential range of −0.8 to 0.1 V in the second cycle.[49] In addition, the CSCc density was obtained by comparing the CSCc with the electrode area. The calculation formula was as follows:

$$CSCc = \frac{1}{vA}\int_{Ec}^{Ea} |i|dE$$

where *A* was the total surface area of electrode, *v* was the scanning rate of CV, *Ea* and *Ec* were the set potentials of the scanning, respectively, and the *I* was the response current.

Bending properties of MoS_2 electrode

Bending stability

Bending stability was assessed by bending 5 mm electrodes by 30°, 90°, and 180° using custom molds, respectively, and then testing the electrochemical impedance of the bent electrodes with a three-electrode system.

Bending stiffness

Bending stiffness was characterized using a Dynamic Mechanical Analyzer (Q800, TA Instruments) in double cantilever mode. Electrodes with a length of 6 cm were mounted on a cantilever clamp, and then were tested with frequency sweeps (0.01–10 Hz) under controlled displacement (100 μm) conditions.

Stability of MoS_2 electrodes

The MoS_2 electrodes were soaking in 15 mL of PBS. The EIS was tested at 1 week intervals or after ultrasound oscillation for 10 min to observe the Long-term stability and mechanical stability of the electrodes. SEM characterization of the electrode surface was performed after stability testing to observe the interface morphology. The soaking solution was subjected to ICP-MS to determine the Mo ion content and to judge whether the coating was dissolved.

Catalytic activity of MoS_2 electrode

Electrocatalytic activity of electrodes

The bare electrode and the MoS_2 electrode were subjected to LSV and CV in PBS containing 10 mM H_2O_2. The LSV scan rate was 5 mV/s and the CV scan rate was 50 mV/s. In the three-electrode system of the electrochemical workstation, the MoS_2 electrodes were the working electrodes, the platinum wire electrode and the saturated calomel electrode were used as the counter electrode and the reference electrode. The electrocatalytic activity of the electrodes was evaluated by comparing the response current density.

Total antioxidant activity tests (ABTS rapid method)

The total antioxidant activity of the electrodes was assayed by the ABTS rapid method and the procedure was carried out according to the instructions of the kit. The absorbance of the same volume of sample at 414 nm was determined using the UV-vis spectrophotometer. The concentration of $ABTS^{\bullet+}$ was obtained from the Lambert-Beer law (the molar extinction coefficient of $ABTS^{\bullet+}$: $\epsilon_{414\ nm} = 3.6 \times 10^4\ mol^{-1}\ cm^{-1}$) during the analysis of reaction kinetics.

In vitro cytotoxicity assay of MoS_2 electrode

HT22 cells were obtained from the Institute of Radiation Medicine, Chinese Academy of Medical Sciences, and used for all *in vitro* cytotoxicity assays. The cell culture medium was Dulbecco's Modified Eagle Medium (DMEM) (Gibco) with 10% fetal bovine serum (FBS, BI). In all, 100 U/mL penicillin and 100 mg/mL streptomycin sulfate (Solomo) were applied according to the growth state.

Direct contact cytotoxicity test

HT22 cells (1×10^5) were cultured in 24-well plates in 1 mL culture medium and incubated in the cell culture incubator (5% CO_2, at 37°C) for 24 h. The electrodes were sterilized and cleaned, and cut into 1-cm electrode segments and placed into the cell culture wells. Cells were stained using Calcein/PI Cell Live/Dead Viability/Cytotoxicity Assay Kit (Beyotime, C2015S) after incubation for 24 and 48 h, in which Calcein Acetoxymethyl Ester (Calcein AM) fluorescently stained live cells (green) and Propidium Iodide (PI) stained dead cells (red). Detailed operations were described in the kit instructions. The distribution of live and dead cells after staining was visualized using fluorescence microscopy.

Indirect contact cytotoxicity test

Bare electrodes and MoS_2 electrodes of identical size were immersed in equal volumes of cell culture medium and placed in the cell culture incubator for 24 h. The extracts were then added to 96-well plates seeded with HT22 cells (3×10^3). After 12, 24, 36, and 48 h of incubation, Cell Counting Kit-8 (CCK-8) (APExBIO, K1018, USA) solution was added and incubated for 1 h, and the absorbance of the supernatant was

measured at 450 nm using a spectrophotometer. The control group was subjected to the identical test without any electrodes, and cell viability was normalized.

Implantation surgery of MoS_2 electrode

Adult male Wistar rats (250–280 g) were housed under standard conditions, with *ad libitum* access to food and water. Before the start of the operation, anesthetize rats using isoflurane (5% for induction, 0.5–1.5% for maintenance). The rat's head was then shaved and fixed on a stereotaxic frame with toothed racks and ear bars, and the scalp was incised with a scalpel to expose the skull and then the cranial window was opened using a cranial drill. The bare electrodes and MoS_2 electrodes were slowly inserted into the hippocampal CA3 area of the symmetrical brain region of the rat (3.5 mm lateral and 2.5 mm posterior to bregma; 2 mm depth from the dura mater) using a stereotactic frame, and two stainless-steel screws were implanted to serve as the grounding electrode and the reference electrode. All experiments were performed in accordance with the Animal Management Rules of the Ministry of Health of the People's Republic of China and were reviewed by the Animal Ethics and Welfare Institute.

In vivo neural recording of MoS_2 electrode

The MoS_2 electrode and the control electrode were immersed in the aCSF to simulate the tissue fluid environment, and the noise level was tested without any neural signal input, including thermal noise and environmental noise introduced by the system. After the aCSF was stabilized, the background noise referenced to ground was recorded by the electrodes. The noise level was sampled at 30 kHz using Intan system (M4200, USA) and then was filtered in the range of 0.5–100 Hz with offline using custom routines in MATLAB (MathWorks). The noise signals were shown in time and frequency domains, and the power spectra with frequency range of 1 Hz–100 Hz were presented.

Rats with implanted electrodes were connected to the Intan system (M4200, USA) via specific connectors to record the LFP. The signal was recorded digitally at a sampling rate of 30 kHz for at least 30 min per acute recording. The acquired LFP signals were intercepted in a 20 s window and band-pass filtered from 1 to 50 Hz, and then the power spectrum was plotted by FFT. Multi-band band-pass filtering was applied to the LFP signal to categorize it into five bands: δ (1–4 Hz), θ (4–8 Hz), α (8–14 Hz), β (14–30 Hz) and γ (30–50 Hz), and the time domain plots of different frequency bands were plotted and their energies are calculated. The phase synchronization of the LFP signals acquired from the bare and MoS_2 electrodes was analyzed by the WPLI calculation using the formula:

$$\mathrm{WPLI} = \frac{|E(\partial(x))|}{E(|\partial(x)|)} = \frac{|E(|\partial(x)|\mathrm{sgn}(\partial(x)))|}{E(|\partial(x)|)}$$

x is the cross spectrum of the two signals, $\partial(x)$ is the imaginary component of the cross-spectrum, E(.) is the expected value operator. The WPLI results range between 0 and 1, where values closer to 1 indicate higher phase synchronization and stronger coupling. Random signal matching experiment is performed by labeling each segment of electrophysiological signals with a serial number and then using a randomized algorithm to generate matching sequences and calculate the WPLI. All the analyses performed on the LFP signals were implemented using MATLAB code.

Biocompatibility of MoS_2 electrode

One week after electrode implantation, the rats were anesthetized and perfused with PBS followed by paraformaldehyde (PFA), and their fresh brains were collected. The brains were fixed in 30 mL of PFA for 24 h, then dehydrated in a gradient using 10%, 20%, and 30% sucrose solutions, and embedded in optimal cutting temperature (OCT) compounds (Tissue-Tek, USA). The brains were then cut into 20 μm sections and mounted on glass slides (stored at -80°C). For staining, the brain sections were brought to room temperature, washed with PBS, then treated for 30 min with 0.3% (v/v) Triton X-100 in PBST (0.1% Tween 20 in 1x PBS) and 10% donkey serum. Excess liquid was removed, and primary antibodies including GFAP (Abcam, ab4648, 1:10), Iba1 (Thermo, MA5-27726, 1:100), and NeuN (CST, 94403S, 1:100) were applied and incubated overnight at 4°C. The sections were washed with PBS to remove excess primary antibody solution, and then secondary antibodies were added in a light-protected environment, including CoraLite488-conjugated Affinipure Donkey Anti-Rabbit IgG (H + L) (Proteintech, SA00013-6, 1:100), and Donkey Anti-Mouse IgG H&L (Alexa Fluor 594) (Abcam, ab150108, 1:100). After incubating for 100 min, the excess secondary antibodies were washed off with PBS. Finally, the nuclei were stained with DAPI, and the sections were imaged using a confocal microscope. Quantitative analysis of the immunofluorescence graphs was performed using ImageJ, which was implemented by a program script that calculates the fluorescence intensity of the biomarker inside the circle with a radius step of 25 μm from the center of the circle as the center of the electrode implantation position and normalizes it. The size of the neuron lost zone was defined as twice the distance from the electrode implantation center to the site where the fluorescence intensity was below 80% of the background value. The graphical abstract were partially created with BioRender.com.

QUANTIFICATION AND STATISTICAL ANALYSIS

All data were presented as mean $\pm$ standard deviation (SD) from at least three separate experiments. Statistical tests of the data were performed using the Kruskal-Wallis test, t-test and one-way ANOVA to obtain a *p*-value (n.s.: not significant, $*p < 0.05$, $**p < 0.01$, $***p < 0.001$). Statistical analyses and graphs were performed using the OriginPro 8.0, SPSS 27 and MATLAB R2013b.